CORE
Metadata, citation and similar papers at core.ac.uk
Provided by Caltech Authors

MNRAS **454,** 1310–1319 (2015) doi:10.1093/mnras/stv2091

Parameter constraints in a near-equipartition model with multifrequency *NuSTAR*, *Swift*, and *Fermi*-LAT data from 3C 279

Dahai Yan,[1⋆] Li Zhang[2⋆] and Shuang-Nan Zhang[1⋆]

[1]*Key Laboratory of Particle Astrophysics, Institute of High Energy Physics, Chinese Academy of Sciences, Beijing 100049, China*
[2]*Department of Astronomy, Key Laboratory of Astroparticle Physics of Yunnan Province, Yunnan University, Kunming, 650091, China*

Accepted 2015 September 7. Received 2015 September 4; in original form 2015 June 23

ABSTRACT

Precise spectra of 3C 279 in the 0.5–70 keV range, obtained during two epochs of *Swift* and *NuSTAR* observations, are analysed using a near-equipartition model. We apply a one-zone leptonic model with a three-parameter log-parabola electron energy distribution to fit the *Swift* and *NuSTAR* X-ray data, as well as simultaneous optical and *Fermi*-LAT gamma-ray data. The Markov chain Monte Carlo technique is used to search the high-dimensional parameter space and evaluate the uncertainties on model parameters. We show that the two spectra can be successfully fitted in near-equipartition conditions, defined by the ratio of the energy density of relativistic electrons to magnetic field ζ_e being close to unity. In both spectra, the observed X-rays are dominated by synchrotron self-Compton photons, and the observed gamma-rays are dominated by Compton scattering of external infrared photons from a surrounding dusty torus. Model parameters are well constrained. From the low state to the high state, both the curvature of the log-parabola width parameter and the synchrotron peak frequency significantly increase. The derived magnetic fields in the two states are nearly identical ($\sim$1 G), but the Doppler factor in the high state is larger than that in the low state ($\sim$28 versus $\sim$18). We derive that the gamma-ray emission site takes place outside the broad-line region, at $\gtrsim$0.1 pc from the black hole, but within the dusty torus. Implications for 3C 279 as a source of high-energy cosmic rays are discussed.

Key words: radiation mechanisms: non-thermal – galaxies: jets – gamma-rays: galaxies.

1 INTRODUCTION

Blazar emission is generally dominated by non-thermal radiation over all frequencies ranging from radio to TeV gamma-rays. By modelling blazar spectra, mechanisms and physical properties of the relativistic jets can be determined. The typical multiwavelength spectral energy distribution (SED) of a blazar is characterized by two distinct humps. It is generally accepted that the first hump in the blazar SED is non-thermal synchrotron emission radiated by relativistic electrons in the jet. The origin of the emission in the gamma-ray hump is less certain. Leptonic and hadronic models have both been proposed to explain the formation of the second bump (see e.g. Böttcher, Harris & Krawczynski 2012, for review). In general, both types of models are able to reproduce the SEDs well, but require quite different jet properties, with the hadronic models sometimes requiring super-Eddington jet powers (Böttcher et al. 2013; Zdziarski & Böttcher 2015). The leptonic models are more attractive by allowing much smaller jet powers, and by more readily explaining rapid blazar variability from highly radiative electrons in contrast to the more weakly radiating hadrons (cf. Cerruti et al. 2015).

All hadronic models are hybrid lepto-hadronic, because the synchrotron bump is believed to be radiated by directly accelerated electron/lepton primaries in the jet. Besides the leptonic synchrotron self-Compton (SSC) component, gamma-rays in hadronic models can result from proton- or ion-synchrotron radiation (Aharonian 2000; Mücke et al. 2003) and $p\gamma$ interactions, including both photopion and Bethe–Heitler photopair production (Atoyan & Dermer 2001, 2003; Böttcher, Reimer & Marscher 2009; Böttcher et al. 2013; Mastichiadis, Petropoulou & Dimitrakoudis 2013; Dimitrakoudis, Petropoulou & Mastichiadis 2014; Murase, Inoue & Dermer 2014; Weidinger & Spanier 2015; Yan & Zhang 2015). Interactions of ultra-relativistic protons and ions in the jet with photons induce cascades by the injection of extremely high energy photons and leptons.

In leptonic models, gamma-rays are produced via inverse Compton (IC) scattering of the relativistic electrons, including SSC scattering (e.g. Maraschi, Ghisellini & Celotti 1992; Tavecchio, Maraschi & Ghisellini 1998; Finke, Dermer & Böttcher 2008; Yan, Zeng & Zhang 2014) and external Compton (EC) scattering (e.g. Dermer & Schlickeiser 1993; Sikora, Begelman & Rees 1994; Błażejowski et al. 2000; Dermer et al. 2009; Kang, Chen &

⋆ E-mail: yandahai@ihep.ac.cn (DY); lizhang@ynu.edu.cn (LZ); zhangsn@ihep.ac.cn (S-NZ).

© 2015 The Authors
Published by Oxford University Press on behalf of the Royal Astronomical Society

Downloaded from http://mnras.oxfordjournals.org/ at California Institute of Technology on January 31, 2016

Wu 2014; Paliya, Sahayanathan & Stalin 2015). EC models seem to be required for flat-spectrum radio quasars (FSRQs; a subclass of blazars with intense broad-line radiation in the inner jet). Depending on the emission site, the external seed photons could be dominated by radiation from accretion disc (e.g. Dermer, Schlickeiser & Mastichiadis 1992; Dermer & Schlickeiser 1993, 2002), broad-line region (e.g. Sikora et al. 1994; Zhang et al. 2012), and dusty torus (e.g. Błażejowski et al. 2000). Many efforts have been made to locate the gamma-ray emission regions of FSRQs (e.g. Liu & Bai 2006; Bai, Liu & Ma 2009; Tavecchio et al. 2010; Dotson et al. 2012; Yan, Zeng & Zhang 2012; Nalewajko, Begelman & Sikora 2014), but it is still an unresolved issue.

Radio telescopes can partially resolve the structure of blazar jets. The observed connections between gamma-ray flares and radio/millimetre flares are used to argue for gamma-ray emission arising at distance scales of $\gtrsim$pc, or even $\gtrsim$10pc (e.g. Jorstad et al. 2001; Jorstad, Marscher & Larionov 2010; Agudo et al. 2011). However, Tavecchio et al. (2010) argued that the rapid variabilities on time-scale of a few hours challenge the scenario in which gamma-ray emission site is placed at tens of parsec from the black hole. Using the time lags of gamma-rays relative to broad emission lines, Liu, Bai & wang (2011) argued that gamma-ray emission may be produced in the regions of the jet at $\lesssim$2pc from the black hole.

Although blazar emission models have been constructed that accurately reproduce contemporaneous SED data, the number of free parameters in even the simplest SSC model can exceed the number of constraining observables. Therefore, blazar SED modelling generally yields degenerate parameter values, which makes it difficult to investigate correlations between model parameters.

Claims and explanations of correlations between model parameters have been made, for example, for statistical quantities like the blazar sequence (Fossati et al. 1998; Ghisellini et al. 1998), or for flux–flux or flux–index correlations between different spectral states of the same blazar. Due to many free and unconstrained parameters, it is difficult to establish robust correlations between model parameters using simple fitting methods.

Using the Markov chain Monte Carlo (MCMC) technique, Yan et al. (2013) constrained parameter space in an SSC model for Mrk 421. The high-quality SEDs enable us to derive the confidence intervals of each model parameter using the MCMC method, and to do a comparison of model fits for different SEDs. In a series of papers (Yan et al. 2013; Peng, Yan & Zhang 2014; Zhou et al. 2014), we showed that fitting high-quality SEDs with the MCMC technique is a powerful approach to investigating the blazar jet physics. In a related modelling effort, Dermer et al. (2014) assumed that a three-parameter log-parabola function approximates the electron energy distribution (EED). Introducing the equipartition parameter $\zeta_{\rm e} = u'_{\rm e}/u'_{B'}$ as the ratio of the energy densities of electrons $u'_{\rm e}$ and magnetic field $u'_{B'}$ gives, when $\zeta_{\rm e} \approx 1$, the minimum synchrotron jet power. Besides $\zeta_{\rm e}$, the other three equipartition factors in this modelling approach (Cerruti et al. 2013; Dermer et al. 2014) are (1) $\zeta_{\rm s}$, the ratio of the energy density of synchrotron radiation $u'_{\rm syn}$ to $u'_{B'}$; (2) $\zeta_{\rm BLR}$, the ratio of the energy density of BLR radiation in comoving frame $u'_{\rm BLR}$ to $u'_{B'}$; and (3) $\zeta_{\rm dust}$, the ratio of the energy density of dust radiation in comoving frame $u'_{\rm dust}$ to $u'_{B'}$. In this approach, the physical parameters (e.g. fluid magnetic field B' and Doppler factor $\delta_{\rm D}$) are expressed in terms of observables (e.g. synchrotron peak frequency and synchrotron peak luminosity, and variability time-scale). With this formulation, GeV cutoffs in blazar spectra are explained under equipartition conditions by IC scattering BLR radiation in the Klein–Nishina regime (Cerruti et al. 2013). In SSC models, the equipartition modelling approach allows the complete set of parameters to be fully constrained, contingent on the underlying assumption that the electron distribution can be described, at least approximately, by a log-parabola function. Here, we constrain the parameters using the near-equipartition, log-parabola model for 3C 279. In our approach, we do not adopt $\zeta_{\rm BLR}$ and $\zeta_{\rm dust}$ to define the energy densities of the external radiations. Instead, we use the distance r from emitting region to supermassive black hole to deduce the energy densities of the external radiations via the standard scaling relations for BLR and dust torus radiations. We will give the details in Section 2.

The blazar 3C 279, at redshift $z = 0.536$, is classified as an FSRQ due to its strong prominent emission lines, and was one of the first gamma-ray blazars discovered (Hartman et al. 1992). Its synchrotron peak frequency is $<10^{14}$ Hz, making it a low-synchrotron peaked object, like most FSRQs (Ackermann et al. 2011). Rapid variability is observed in 3C 279; the analysis in Paliya (2015) shows that the variability time-scale for GeV emission of 3C 279 can be down to $\sim$1–2 h.

Using the near-equipartition leptonic model with a log-parabola EED, Dermer et al. (2014) satisfactorily explained four SEDs of 3C 279 reported in Hayashida et al. (2012). Since then, detailed simultaneous multiwavelength SED data of 3C 279 in four states of elevated activity that took place between 2013 December and 2014 April were analysed by Hayashida et al. (2015). In particular, Hayashida et al. (2015) reported 0.5–70 keV X-ray spectra obtained from *Swift*-XRT and *NuSTAR* observations in two flaring periods, namely period A, taking place from 2013 December 16–19, and period C, from 2013 December 31–2014 January 3. Hayashida et al. (2015) argue that their one-zone leptonic models with a double-broken power-law EED fail to explain the *Swift*-XRT and *NuSTAR* X-ray spectra.

In this paper, we fit the two simultaneous SEDs that include *NuSTAR* data reported in Hayashida et al. (2015) using the near-equipartition blazar model with a log-parabola EED. Using the MCMC technique, we derive the best-fitting results and the uncertainties on parameters. The implications of the results on the acceleration processes in the jet of 3C 279 are discussed. Supposing that 3C 279 is a high-energy cosmic ray (CR) source, we discuss its implied CR luminosity. We use parameters $H_0 = 71\ {\rm km\ s^{-1}\ Mpc^{-3}}$, $\Omega_{\rm m} = 0.27$, and $\Omega_\Lambda = 0.73$.

2 EMISSION MODEL AND FITTING TECHNIQUE

In the log-parabola leptonic blazar model (Dermer et al. 2014), the non-thermal electron distribution is assumed to be isotropic in the emission region (blob), and described by a log-parabola function

$$\gamma'^2 N'_{\rm e}(\gamma') \sim \left(\frac{\gamma'}{\gamma'_{\rm pk}}\right)^{-b\ \log(\gamma'/\gamma'_{\rm pk})}, \quad (1)$$

where γ' is the electron Lorentz factor, b is the spectral curvature parameter, and $\gamma'_{\rm pk}$ is the peak Lorentz factor in the $\gamma'^2 N'_{\rm e}(\gamma')$ distribution. Emission from the blob is strongly boosted due to the beaming effect. Besides SSC emission, EC components for low-energy target photons from the BLR (EC-BLR) and the dusty torus (EC-dust) are included.

As mentioned in Section 1, we do not use the equipartition relations $\zeta_{\rm BLR}$ and $\zeta_{\rm dust}$ (Cerruti et al. 2013; Dermer et al. 2014) to normalize the energy densities of the external radiations. We take the distance r from the central black hole to the emitting blob as

Downloaded from http://mnras.oxfordjournals.org/ at California Institute of Technology on January 31, 2016

an input parameter. The energy densities of BLR radiation ($u_{\rm BLR}$) and dust radiation ($u_{\rm dust}$) can be expressed as functions of r (Sikora et al. 2009; Hayashida et al. 2012)

$$u_{\rm BLR}(r) = \frac{\tau_{\rm BLR} L_{\rm disc}}{4\pi r_{\rm BLR}^2 c[1+(r/r_{\rm BLR})^3]}, \quad (2)$$

$$u_{\rm dust}(r) = \frac{\tau_{\rm dust} L_{\rm disc}}{4\pi r_{\rm dust}^2 c[1+(r/r_{\rm dust})^4]}. \quad (3)$$

The size of BLR is related to the disc luminosity $L_{\rm disc}$: $r_{\rm BLR} = 10^{17}(L_{\rm disc}/10^{45}\ {\rm erg\ s^{-1}})^{1/2}$cm (Ghisellini & Tavecchio 2009; Ghisellini et al. 2014). We assume a dust torus with the size of $r_{\rm dust} = 10^{18}(L_{\rm disc}/10^{45}\ {\rm erg\ s^{-1}})^{1/2}$cm. This size of dust torus is half of the size used in Ghisellini et al. (2014), which enhances the energy density of dust radiation. Using the scalings between $L_{\rm disc}$ and $r_{\rm BLR/dust}$, we can rewrite equations (2) and (3) as

$$u_{\rm BLR}(r) \simeq \frac{0.3\tau_{\rm BLR}}{1+(r/r_{\rm BLR})^3}\ {\rm erg\ cm^{-3}}, \quad (4)$$

$$u_{\rm dust}(r) \simeq \frac{0.003\tau_{\rm dust}}{1+(r/r_{\rm dust})^4}\ {\rm erg\ cm^{-3}}, \quad (5)$$

where $\tau_{\rm BLR}$ and $\tau_{\rm dust}$ are the fractions of the disc luminosity reprocessed into BLR radiation and into dust radiation, respectively. We adopt the typical values of $\tau_{\rm BLR} = 0.1$ (e.g. Ghisellini et al. 2014) and $\tau_{\rm dust} = 0.3$ (e.g. Hao et al. 2005; Malmrose et al. 2011). Using equations (4) and (5), one can obtain $u_{\rm BLR}({\rm erg\ cm^{-3}}) \lesssim 0.3\tau_{\rm BLR}$ and $u_{\rm dust}({\rm erg\ cm^{-3}}) \lesssim 3\tau_{\rm dust} \times 10^{-3}$. The two energy densities are limited by $r_{\rm BLR}$ and $r_{\rm dust}$, respectively. When r is smaller than $r_{\rm dust}$, $u_{\rm dust}$ varies by a factor of at most 2. Moreover, the energy density of the IR dust radiation should be lower than the energy density of a blackbody with the temperature of $T_{\rm dust}$, namely $u_{\rm dust} < u_{\rm bb}(T_{\rm dust}) \backsimeq 3 \times 10^{-4}(T_{\rm dust}/440\ {\rm K})^4$.

The external radiation is assumed to be a dilute blackbody radiation, namely a blackbody spectral shape normalized to $u_{\rm BLR/dust}$. BLR radiation is dominated by Lyα line photons. We adopt an effective temperature for the BLR radiation of $T_{\rm BLR} = 6.3 \times 10^4$K, so that the energy density of BLR radiation peaks at $\approx 2.82 k_{\rm B} T/h \cong 3.7 \times 10^{15}$ Hz in the $u(\nu)$ distribution (Tavecchio & Ghisellini 2008). We consider IR dust radiation with $T_{\rm dust} = 800$K. Note that Dermer et al. (2014) approximated the BLR and dust photon fields as monochromatic. Cerruti et al. (2013) considered a complex of atomic emission lines in BLR. The different approximations for the BLR and dust radiations do not significantly modify the modelling results.

The input parameters in the model are (i) $L_{48} = L_{\rm syn}/10^{48}\ {\rm ergs^{-1}}$, the apparent isotropic bolometric synchrotron luminosity; (ii) $\nu_{14} = (1+z)\nu_{\rm syn}^{\rm obs}/10^{14}$ Hz, the synchrotron peak frequency in the source frame, where $\nu_{\rm syn}^{\rm obs}$ is the measured synchrotron peak frequency; (iii) $t_4 = t_{\rm obs,\ var}/[(1+z)10^4\ {\rm s})]$, the source variability time-scale, where $t_{\rm obs,\ var}$ is the minimum measured variability time-scale; as already noted, we define the equipartition parameter (iv) $\zeta_{\rm e} = u'_{\rm e}/u'_B$; (v) $\zeta_{\rm s} = u'_{\rm syn}/u'_B$, the ratio between the synchrotron photon ($u'_{\rm syn}$) and magnetic-field energy densities; (vi) b, curvature parameters of EED; (vii) r, the location of emitting blob along the jet; (viii) $T_{\rm dust}$, the temperature of dust torus IR radiation; and (ix) $L_{\rm disc}$, accretion disc luminosity.

There are six output parameters: (1) Doppler factor $\delta_{\rm D}$; (2) fluid magnetic-field strength B'; (3) $\gamma'_{\rm pk}$; (4) $u_{\rm BLR}$; (5) $u_{\rm dust}$; and (6) comoving radius of emitting blob, $R' = c\delta_{\rm D} t_{\rm obs,\ var}/(1+z)$. The physical model parameters, $\delta_{\rm D}$, B', and $\gamma'_{\rm pk}$, are deduced by using the equations in Dermer et al. (2014, 2015). The SSC and EC emissions are calculated using the methods given in Dermer et al. (2009). Synchrotron self-absorption (SSA) is included. The contribution of thermal emission is included, which is assumed to be from a Shakura–Sunyaev disc, using the expression following equation (9) in Dermer et al. (2014).

We use the MCMC technique to do the fitting (see details in Yuan et al. 2011; Liu et al. 2012; Yan et al. 2013). The MCMC method, based on the Bayesian statistics, is a powerful tool for high-dimensional parameter space investigation. The Metropolis–Hastings sampling algorithm which ensures that the probability density functions of model parameters can be asymptotically approached with the number density of samples is adopted to determine the jump probability from one point to the next in parameter space (Gamerman 1997; Mackay 2003). The MCMC method is also an effective approach for determining uncertainties of model parameters.

3 RESULTS

We consider the SEDs of 3C 279 from simultaneous observations of *Swift*, *NuSTAR*, and *Fermi*-LAT in two periods reported in Hayashida et al. (2015), namely period A (2013 December 16–19) and period C (2013 December 31–2014 January 3). Since an X-ray spectrum is lacking in period B and there are no *NuSTAR* data in period D, we do not consider these SEDs. Note that the X-ray flux increased by a factor of $\approx$2 and the gamma-ray flux increased by a factor of $\approx$3 from period A to period C.

The X-ray flux showed no intraday variations in period A, but showed intraday variations in period C (Hayashida et al. 2015). Therefore, the variability time-scale for period A is taken to be $t_4 = 5$ which corresponds to an observed variability time-scale of $\sim$21 h, and the variability time-scale for period C is set to be $t_4 = 1$ which corresponds to an observed variability time-scale of $\sim$4 h.

There is no evidence for a thermal emission feature in the two SEDs, making it difficult to constrain the accretion disc luminosity $L_{\rm disc}$. We adopt $L_{\rm disc} = 1.5 \times 10^{45}\ {\rm erg\ s^{-1}}$, which is the maximum disc luminosity allowed by the optical–UV SED. Using this value, we derive $r_{\rm BLR} \simeq 0.04$pc and $r_{\rm dust} \simeq 0.4$pc.

By comparison, at a much earlier three-week epoch between December 1992 and January 1993, Pian et al. (1999) originally discovered the accretion disc emission from 3C 279 during a low-state monitored with *ROSAT*, *IUE*, and EGRET, finding a νF_ν flux of $\approx 3 \times 10^{-12}$ erg s^{-1} cm^{-2} between $\approx$1 and 2×10^{15} Hz, corresponding to a UV luminosity $L_{\rm disc} = 2.4 \times 10^{45}\ {\rm erg\ s^{-1}}$.

Due to the strong SSA below 10^{12} Hz, we fit only the optical, X-ray, and gamma-ray data, but not the 230 GHz SMA point.

Fig. 1 shows the best-fitting to the SED of 3C 279 for period A. The fit is satisfactory. The joint *Swift* and *NuSTAR* X-ray spectrum is successfully fitted, and is dominated by the SSC component. The gamma-ray emission is dominated by the EC-dust component.

In Fig. 2, we give the one-dimensional probability distributions and the two-dimensional contours of input and output parameters. The complete information on constraining parameters can be read from this figure. We note that $\zeta_{\rm e}$ is constrained in the range of [0.8–1.7] (the marginalized 95 per cent confidence interval). The distance r is constrained in the range of [0.1–0.4] pc, namely the emitting blob is outside the BLR, but is still inside the dust torus ($r_{\rm BLR} \simeq 0.04$pc and $r_{\rm dust} \simeq 0.4$pc). The derived $u_{\rm dust}$ is in the range of [5–9] $\times 10^{-4}$ erg cm^{-3}, and $u_{\rm BLR}$ is in the range of [0.2–10] $\times 10^{-4}$ erg cm^{-3}. The magnetic field B' is in the range of [0.7–1.2] G, and $\delta_{\rm D}$ is in the range of [17–20]. We summarize the marginalized

Downloaded from http://mnras.oxfordjournals.org/ at California Institute of Technology on January 31, 2016

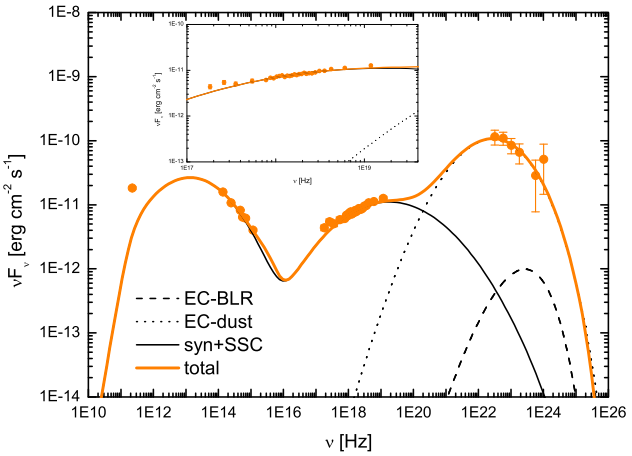

Figure 1. Best-fitting model to the SED of 3C 279 for period A (data from Hayashida et al. 2015). The inset shows the details of fit at X-ray energies.

95 per cent confidence intervals for input and output parameters in Table 1. We also notice that there is a correlation between r and ζ_e, and B' is anti-correlated with δ_D (see the two-dimensional contours). These parameter correlations showed in Fig. 2 are caused by degeneracies of the leptonic model (e.g. Tavecchio et al. 1998; Sikora et al. 2009; Dermer et al. 2014). Nevertheless, all parameters except u_{BLR} are well constrained.

The fit to the SED from period C is also satisfactory (Fig. 3). The *Swift–NuSTAR* X-ray spectrum from period C shows a break at 3.7 keV with photon indices of 1.37 and 1.76, respectively, below and above the break energy, when fitted by a broken power law (Hayashida et al. 2015). Our results show that the one-zone leptonic model can successfully fit the X-ray spectrum. The X-ray emission in period C is almost entirely attributed to SSC, and the spectral break is naturally explained. The gamma-ray emission is again dominated by the EC-dust component.

The one-dimensional probability distributions and the two-dimensional contours of input and output parameters derived in the fitting to the SED for period C are shown in Fig. 4. In this period, the gamma-ray emission site r is in the range of [0.1–0.4] pc, identical to that in period A, but a larger ζ_e of [3–5] and δ_D of [26–30] are required to explain the higher gamma-ray flux. The magnetic field B' of [0.9–1.4] is nearly identical to that in period A. From period A to period C, ζ_s and ν_{14} increase, respectively, from ∼0.5 to 0.8 and from ∼0.3 to 0.5, and b increases from ∼1.2 to 1.5.

In Table 1, we also give the jet powers for a two-sided jet in the form of radiation (P_r), Poynting flux (P_B), where we assume that Doppler factor is related to the bulk Lorentz factor through $\delta_D = \Gamma$. The relativistic emitting electron power P_e, which is not shown, is obtained from the relation $P_e = \zeta_e P_B$. This is the minimum jet power, and the addition of hadrons will only increase this power. One can see that the radiation power P_r is significantly greater than P_B and P_e in both cases.

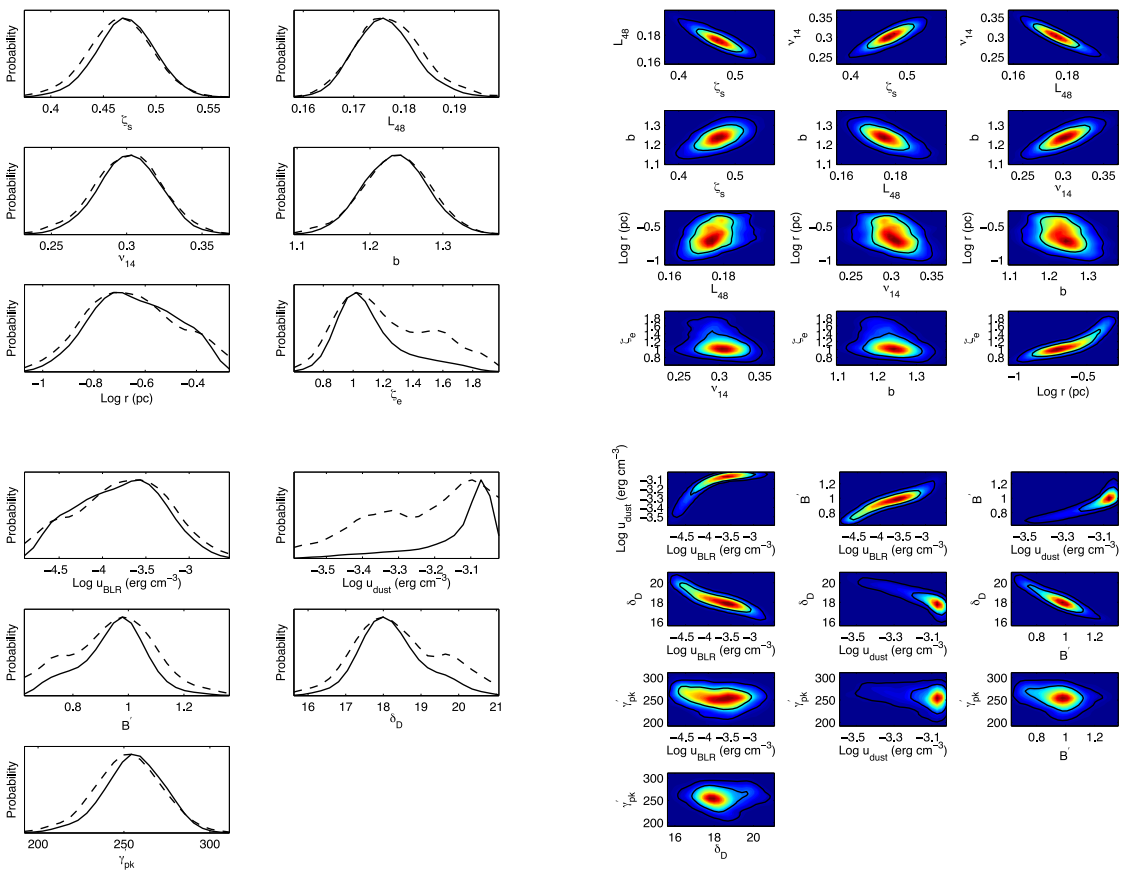

Figure 2. One-dimensional probability distribution of parameter values (left; the dashed curves are the mean likelihoods of samples and the solid curves are the marginalized probabilities) and two-dimensional contours of parameters [right; the regions enclosing the 68 per cent (95 per cent) confidence level are shown] for period A. The upper panel is for the input parameters, and the lower panel is for the output parameters.

Downloaded from http://mnras.oxfordjournals.org/ at California Institute of Technology on January 31, 2016

Table 1. Input and output parameters values. The mean values and the marginalized 95 per cent confidence intervals (CI) for interested parameters are reported.

					Input				
	ζ_e	b	L_{48}	ν_{14}	t_4	ζ_s	r (pc)	T_{dust} (K)	L_{disc} (10^{46} erg s^{-1})
Period A	1.12	1.24	0.18	0.30	5	0.47	0.2	800	0.15
(95 per cent CI)	0.80–1.71	1.15–1.32	0.17–0.19	0.26–0.34	–	0.41–0.52	0.1–0.4		–
Period C	4.06	1.49	0.23	0.54	1	0.81	0.3	800	0.15
(95 per cent CI)	3.04–5.0	1.43–1.57	0.22–0.24	0.50–0.58	–	0.74–0.89	0.1–0.4		–
					Output				
	B (G)	δ_D	γ'_{pk}	u_{dust} (10^{-3} erg cm^{-3})	u_{BLR} (10^{-3} erg cm^{-3})	R' (10^{16} cm)	P_B (10^{45} erg s^{-1})	P_r (10^{46} erg s^{-1})	
Period A	1.0	18	260	0.7	0.2	2.7	1.7	2.0	
(95 per cent CI)	0.7–1.2	17–20	220–290	0.5–0.9	0.02–1	–	–	–	
Period C	1.1	28	300	0.6	0.1	0.8	0.5	1.3	
(95 per cent CI)	0.9–1.4	26–30	280–310	0.5–0.9	0.03–2	–	–	–	

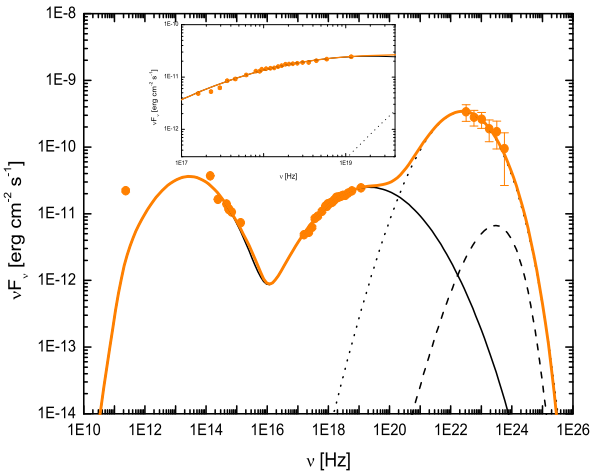

Figure 3. Best-fitting model to the SED of 3C 279 for period C (data from Hayashida et al. 2015). The inset shows the details of fit at X-ray energies.

4 DISCUSSION AND CONCLUSIONS

A one-zone leptonic model with a three-parameter log-parabola EED (Dermer et al. 2014) is used to fit the two SEDs of 3C 279 where joint *NuSTAR* and *Swift* data are available (the SEDs from period A and period C in Hayashida et al. 2015). Using the MCMC method, we obtained the best-fitting results and the uncertainties on the input and output parameters. Our results show that the two SEDs can be successfully fitted in near-equipartition conditions. In both cases, the gamma-ray emission is dominated by the EC-dust component, and the EC-BLR component is essentially negligible, and the X-ray emission is dominated by SSC emission. The SSC origin of X-ray emission is expected to be highly polarized if the magnetic field is perpendicular to the line of sight (e.g. Krawczynski 2012). The X-ray measurements of the degree of polarization by future detectors such as X-ray timing and polarization and *ASTRO-H* would give more details on the magnetic field.

We take advantage of the MCMC technique to search the multidimensional parameter space, and to evaluate the uncertainties on the parameters. We have shown that all parameters except u_{BLR} are constrained very well by the current data. The stringently constrained parameters enable us to investigate the important issues in blazar physics confidently.

We derive the energy density of BLR radiation $u_{BLR} < 0.002$ erg cm^{-3} at the 95 per cent confidence level. Our results show that the EC-BLR component is essentially negligible in modelling the two SEDs 3C 279. Note that Cerruti et al. (2013) showed that the EC-BLR component is necessary to explain the GeV break in 3C 454.3. The distance r from gamma-ray emission blob to the black hole is well constrained in the range of [0.1–0.4] pc, namely the gamma-ray emission region is outside the BLR, but is inside the dusty torus. The value of r depends on the assumptions on r_{BLR} and r_{dust}. Compared with the previous works (e.g. Ghisellini & Tavecchio 2009; Hayashida et al. 2012; Ghisellini et al. 2014; Nalewajko et al. 2014), we adopted a smaller r_{dust}. In Appendix A, we show the fitting results with $r_{dust} = 2 \times 10^{18}(L_{disc}/10^{45}$ erg s$^{-1})^{1/2}$cm (Ghisellini et al. 2014). We find that the lower limit of r derived in the fittings with the larger r_{dust} is still 0.1 pc; the upper limit is modified, but is still less than r_{dust}. Therefore, our conclusion on the gamma-ray emission site is still tenable. Our result is consistent with the gamma-ray emission site in 3C 279 derived by Dermer et al. (2014), and is also consistent with the result derived by Nalewajko et al. (2014) who used an independent method to constrain the gamma-ray emission site. Pacciani et al. (2014) explored the emission zone in high-energy flares of 10 FSRQs, and also found the evidence of gamma-ray flares occurring outside the BLR.

The log-parabola EED can be generated by stochastic particle acceleration, for example, through systematic gyro-resonant acceleration of electrons with plasma waves (e.g. Becker, Le & Dermer 2006; Tramacere, Massaro & Taylor 2011; Asano et al. 2014; Kakuwa et al. 2015), and the correlations between the curvature b and the peak energy γ'_{pk} of EED provide evidence about the acceleration process (e.g. Tramacere et al. 2011). By fitting the SEDs, the EEDs are inferred, which helps to identify acceleration processes in the jet (Yan et al. 2013; Peng et al. 2014; Zhou et al. 2014). Indeed, Yan et al. (2013) found that, because of the improved fits with curving rather than power-law EEDs, it is likely that stochastic acceleration is acting in the jet of Mrk 421 in the giant flare state in 2010 February. The acceleration process is also revealed by dynamic changes of the SED, which implies changes in the EED. Yan et al. (2013) also found that for Mrk 421 as ν_{14} increased from ∼1000 in the low state to ∼10 000 in the giant flare, the curvature of power-law log-parabola EED in the $N'(\gamma')$ distribution increased from ∼1.7 to ∼3.8. We discussed that the changes in ν_{14} and the curvature in Mrk 421 are not compatible with a purely

Downloaded from http://mnras.oxfordjournals.org/ at California Institute of Technology on January 31, 2016

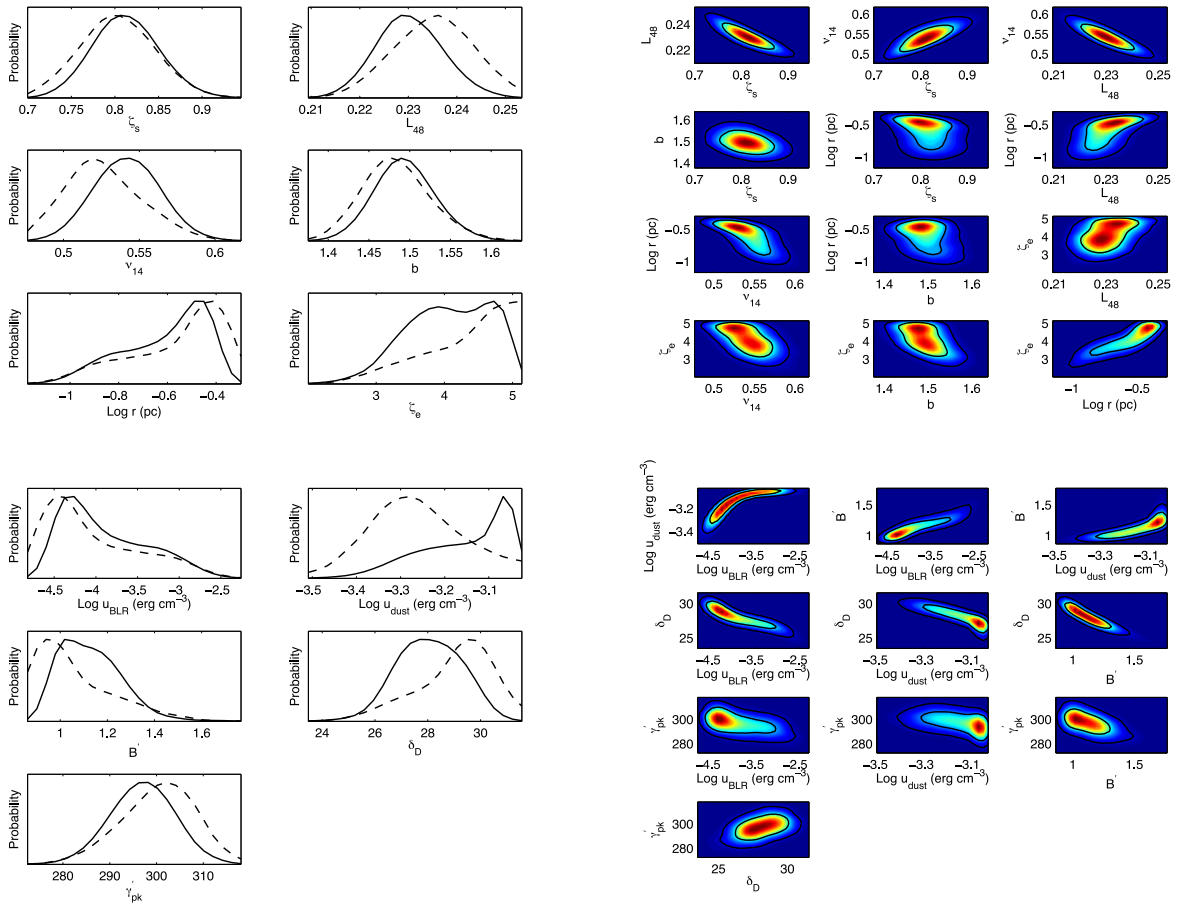

Figure 4. One-dimensional probability distribution of parameter values (left; the dashed curves are the mean likelihoods of samples and the solid curves are the marginalized probabilities) and two-dimensional contours of parameters [right; the regions enclosing the 68 per cent (95 per cent) confidence level are shown] for period C. The upper panel is for the input parameters, and the lower panel is for the output parameters.

acceleration-dominated scenario. The two states of 3C 279 that we have analysed indicate that a changing EED in terms of a changing log-parameter width parameter b plays an important role in different spectral states.

It is known that X-ray spectra of several high-synchrotron-peaked (HSP) BL Lac objects can be described by a log-parabola function (e.g. Massaro et al. 2004a,b). Using a large data set of X-ray observations for several HSPs with $\nu_{14} > 10$, Tramacere, Massaro & Cavaliere (2007), Tramacere et al. (2009), and Massaro et al. (2008) find that the synchrotron peak frequency is anti-correlated with the curvature parameter obtained by fitting the X-ray spectrum. Chen (2014) finds that the synchrotron peak frequency is anti-correlated with the curvature parameter of the synchrotron spectrum for a sample of *Fermi* blazar.

Tramacere et al. (2011) discussed the ν_{14}–b trends in an SSC model with stochastic acceleration. They showed that the anti-correlation between ν_{14} and b for HSPs could be explained in the stochastic acceleration SSC model by a change in the diffusion process rather than by a change of magnetic field that affects the cooling. The radiative cooling of electrons in FSRQs is more efficient than that in HSPs, which may lead to the different ν_{14}–b trend from that for HSPs. Our results show that both ν_{14} and b significantly increase from period A to period C. More high-quality SEDs are needed to confirm the ν_{14}–b trend for FSRQs. Moreover, our results indicate that the gamma-ray emission region is in the dust torus, in contrast to Zhang, Zhang & Liang (2013), who assumed an absence of the dust torus. The unknown gamma-ray emission site may complicate the ν_{14}–b trend for FSRQs. Because of the larger photon energy density in the BLR, radiative cooling of electrons is stronger than that in the dust torus. On the other hand, the relatively inefficient radiative cooling of electrons in the dust tours allows the electrons to be accelerated to higher energies by the inefficient stochastic mechanism.

In our model, the radiation power is much greater than the magnetic-field and relativistic electron power, assuming that the baryon loading (the ratio of the energy density of hadrons to electrons, $\eta_{\rm bl}$) is low, and will not have an impact on the total jet power ($P_{\rm r}$+$P_{\rm B}$+$P_{\rm e}$+$P_{\rm h}$, where $P_{\rm h}$ is the power carried by hadrons) as long as $\eta_{\rm bl} \lesssim 10$. Assuming $\eta_{\rm bl} = 1$, we derive $P_{\rm h} = \eta_{\rm bl} P_{\rm e} = 0.3 \times 10^{46}$ and 0.2×10^{46} erg s^{-1} for period A and period C, respectively. 3C 279 has a black hole with mass (3–8) $\times\ 10^8$ M$_\odot$ (e.g. Gu, Cao & Jiang 2001; Woo & 2002). The Eddington luminosity is therefore in the range (4–10) $\times 10^{46}$ erg s^{-1}. For low baryon loading, the total jet powers in our model are comfortably below the Eddington luminosity of 3C 279.

Blazars are usually considered as CR sources. Using the near-equipartition, log-parabola model, Dermer et al. (2015) gave the following expression for maximum escaping proton energy:

$$E_{\rm max}({\rm eV}) = 1.4 \times 10^{20} L_{48}^{5/16} \left(\frac{t_4}{\nu_{14}}\right)^{1/8} \frac{f_1^{1/4} f_2^{1/8}}{\zeta_{\rm e}^{1/4} \zeta_{\rm s}^{1/16} f_0^{11/16}}\ , \qquad (6)$$

Downloaded from http://mnras.oxfordjournals.org/ at California Institute of Technology on January 31, 2016

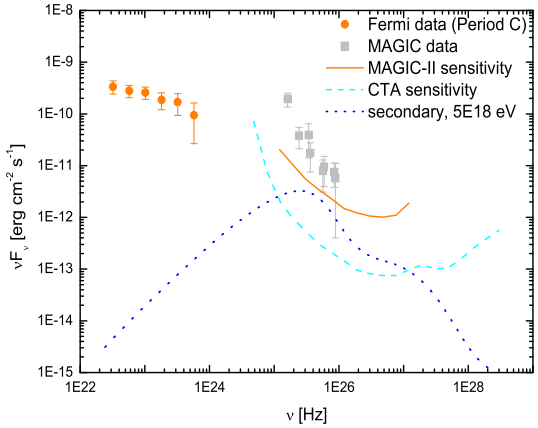

Figure 5. Secondary gamma-ray emission produced in the propagation of CRs. For comparison, the sensitivities of Imaging Atmospheric Cherenkov telescopes (MAGIC-II and CTA) and the non-simultaneous TeV MAGIC data for 3C 279 are shown. The sensitivities and TeV data are obtained through the SED Builder of ASDC (http://tools.asdc.asi.it).

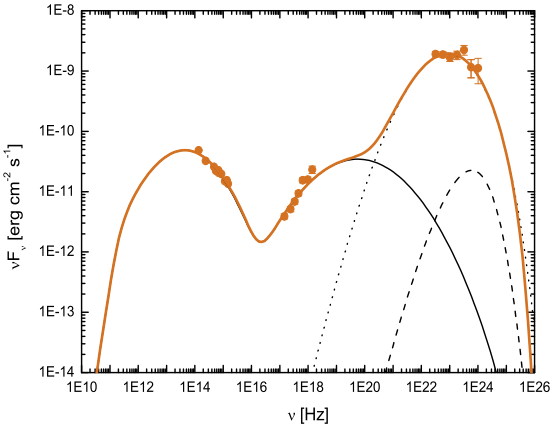

Figure 6. Best-fitting model to the SED of 3C 279 (Hayashida et al. 2015) for period D. The parameter values are $u_{\rm dust} \sim 0.6 \times 10^{-3}$ erg cm^{-3}, $\zeta_{\rm s} \sim 1.0$, $\nu_{14} \sim 0.9$, $b \sim 1.4$, and $L_{48} \sim 0.3$.

with $f_0 = 1/3$, $f_1 = 10^{-1/4b}$, and $f_2 = 10^{1/b}$. Using the best-fitting values for period C (Table 1), we derive $E_{\rm max} \sim 10^{20}$–2×10^{20}eV. However, it should be noted that 3C 279 cannot contribute to the CRs with energy $\gtrsim 10^{18}$eV at the Earth, because of the significant energy losses during the CRs travelling to us.

Besides $E_{\rm max}$, the other key quantity of a blazar is its CR luminosity $L_{\rm CR}$. Secondary gamma-rays are produced when high-energy CRs propagate towards us (e.g. Kalashev, Semikoz & Sigl 2009; Kalashev, Kusenko & Essey 2013), which depends primarily on the values of $L_{\rm CR}$ and $E_{\rm max}$. Such kinds of non-variable secondary emission (variable on time-scale of years; Prosekin et al. 2012) have been proposed to explain the steady VHE ($\gtrsim$100 GeV) emission from distant blazars (e.g. Essey et al. 2010, 2011b; Murase et al. 2012; Aharonian et al. 2013; Takami, Murase & Dermer 2013; Yan et al. 2015).

If 3C 279 emits high-energy CRs, the secondary emission should be lower than its VHE emission, which puts an upper limit on $L_{\rm CR}$. There are no recently reported VHE observations for 3C 279, so we use the sensitivity of MAGIC-II as the upper limit of secondary emission. In Fig. 5, we show the secondary gamma-ray spectrum calculated by using the code TRANSPORTCR (Arisaka et al. 2007; Gelmini, Kalashev & Semikoz 2012; Kalashev & Kido 2014) and the EBL model of Franceschini, Rodighiero & Vaccari (2008, see Finke, Razzaque & Dermer 2010 for detailed comparisons for various EBL models). In the calculation, we assume a log-parabola CR distribution with $b = 1.48$ and peak energy $E_{\rm pk} = 5 \times 10^{18}$ eV, and let the intergalactic magnetic-field strength $B_{\rm IGMF} = 10^{-15}$G (e.g. Essey, Ando & Kusenko 2011a) and its coherence length $\lambda_{\rm coh} = 1$Mpc. To make the secondary emission lower than the sensitivity of MAGIC-II, the CR luminosity is required to be $<6 \times 10^{46}$ erg s^{-1}, significantly lower than $L_{\rm syn}$ and the apparent gamma-ray luminosity ($\sim 10^{48}$ erg s^{-1}). The upper limit of the corresponding absolute CR power $L^{+}_{\rm ab,CR}$ is $\sim 10^{44}$ erg s^{-1} (adopting $\delta_{\rm D} = 28$ in period C), a quarter of $P_{\rm B}$ ($P_{\rm B}$ is for a two-sided jet) in period C. In Fig. 5, it can be seen that Cherenkov Telescope Array (CTA), having significantly improved sensitivity over the present imaging air Cherenkov arrays, will put stronger constraints on the CR luminosity. The upper limit assumes that ultra-high-energy cosmic rays (UHECRs) are not deflected and isotropized during transit, which is unlikely unless the blazar is found in structured regions, for example, clusters and filaments (Murase et al. 2012). Even if the UHECRs can freely escape from the source region, they can be deflected during transport across intergalactic space (Takami, Murase & Dermer 2014).

If the hadrons in the jet are relativistic CRs, as discussed above, these protons could, before escaping from the emission region, lose energies and produce secondary radiations via synchrotron and photohadronic interactions with low-energy photons (e.g. Dermer, Murase & Inoue 2014; Murase et al. 2014). However, the emission made by the protons in the emission region is negligible compared to the observed data, because the proton power ($P_{\rm h}$) in our model is two to three orders of magnitude below the proton power required by hadronic model interpretations of FSRQ SEDs (10^{47}–10^{49} erg s^{-1}) and the magnetic field in our model is one to two orders of magnitude below that usually found in hadronic models (10–100 G; Böttcher et al. 2013; Diltz, Böttcher & Fossati 2015).

In this paper, we fitted the SEDs for period A and period C reported by Hayashida et al. (2015) with our one-zone leptonic model. This model can also explain the SED in the bright flare state of period D with $F(>100$ MeV) of 10^{-5} photons cm^{-2} s^{-1} and $t_{\rm obs,var} \sim 2$h reported by Hayashida et al. (2015). In Fig. 6, we show our best-fitting result for the SED of period D in Hayashida et al. (2015). In this fit, we use $t_4 = 0.5$ and $T_{\rm dust} = 800$K. The best-fitting model requires $\zeta_{\rm e} \sim 10$ and $r \sim 0.2$pc. The deduced parameters are $B \sim 0.8$G, $\delta_{\rm D} \sim 42$, $\gamma'_{\rm pk} \sim 360$, and $R' \sim 6 \times 10^{15}$cm (see the other parameters values in the caption in Fig. 6). The results of period D, compared with those of periods A and C, are consistent with b and ν_{14} mutually increasing. In contrast, the HSP BL Lacs with large peak synchrotron frequencies have broader widths of the synchrotron SEDs (corresponding to smaller values of b) than FSRQs with smaller values of $\nu_{\rm s}$ (Chen 2014).

Because of the lack of X-ray spectrum and the poor data coverage of the synchrotron hump in period B, we do not fit the SED in period B. We found that the EC-dust emission in our model could account for the very hard gamma-ray spectrum ($\Gamma_\gamma \simeq 1.7$) in period B with $\nu_{14} \sim 2.6$, $L_{48} \sim 0.07$, $b \sim 1.7$, $\zeta_{\rm e} \sim 3$, $t_4 \sim 0.5$, and $r \sim 0.3$pc, and we derived $B \sim 0.3$G, $\delta_{\rm D} \sim 60$, $\gamma'_{\rm pk} \sim 950$, and $u_{\rm dust} \sim 0.6 \times 10^{-3}$ erg cm^{-3}.

In conclusion, we have applied the MCMC technique developed for blazar studies by Yan et al. (2013) to the high-quality simultaneous data of 3C 279 (Hayashida et al. 2015), using a log-parabola

Downloaded from http://mnras.oxfordjournals.org/ at California Institute of Technology on January 31, 2016

EED (Dermer et al. 2014). We find that the gamma-ray SED is dominated by the dusty torus radiation, whereas the contribution of the BLR radiation field is very weak. This allows us to place the gamma-ray emission region outside the BLR, at $\gtrsim$0.1 pc, but within the IR radiation field of the torus. The reasonable fits obtained with curving particle distributions are more simply explained with a stochastic acceleration mechanism. The allowed parameter range in 3C 279 is well constrained at different epochs, and shows a positive correlation of the log-parabola width parameter b with peak synchrotron frequency ν_s. Analysis of more FSRQ SEDs will be required to determine if this correlation is robust.

ACKNOWLEDGEMENTS

We would like to give special thanks to Charles Dermer, who carefully edited the manuscript and gave us many valuable suggestions and comments. We thank Charles Dermer, J. Finke, Kinwah Wu for discussions, and the anonymous referee for very helpful and constructive questions. We are grateful to Krzysztof Nalewajko for providing us the data of 3C 279. This work is partially supported by the National Natural Science Foundation of China (NSFC 11433004) and Top Talents Program of Yunnan Province, China. DHY acknowledges partial funding support by China Postdoctoral Science Foundation under grant no. 2015M570152. SNZ acknowledges partial funding support by 973 Program of China under grant 2014CB845802, by the National Natural Science Foundation of China (NSFC) under grant nos. 11133002 and 11373036, by the Qianren start-up grant 292012312D1117210, and by the Strategic Priority Research Program 'The Emergence of Cosmological Structures' of the Chinese Academy of Sciences (CAS) under grant no. XDB09000000. We acknowledge the use of the ASDC web tools (SED Builder, http://tools.asdc.asi.it).

REFERENCES

Ackermann M. et al., 2011, ApJ, 743, 171
Agudo I. et al., 2011 ApJ, 726, L13
Aharonian F. A., 2000, New Astron., 5, 337
Aharonian F., Essey W., Kusenko A., Prosekin A., 2013, Phys. Rev. D, 87, 063002
Arisaka K., Gelmini G. B., Healy M., Kalashev O., Lee J., 2007, J. Cosmol. Astropart. Phys., 12, 002
Asano K., Takahara F., Kusunose M., Toma K., Kakuwa J., 2014, ApJ, 780, 64
Atoyan A., Dermer C. D., 2001, Phys. Rev. Lett., 87, 221102
Atoyan A. M., Dermer C. D., 2003, ApJ, 586, 79
Bai J. M., Liu H. T., Ma L., 2009, ApJ, 699, 2002
Becker P., Le T., Dermer C., 2006, ApJ, 647, 539
Błażejowski M., Sikora M., Moderski R., Madejski G. M., 2000, ApJ, 545, 107
Böttcher M., Reimer A., Marscher A. P., 2009, ApJ, 703, 1168
Böttcher M., Harris D. E., Krawczynski H., eds, 2012, Relativistic Jets from Active Galactic Nuclei. Wiley, Berlin
Böttcher M., Reimer A., Sweeney K., Prakash A., 2013, ApJ, 768, 54
Cerruti M., Dermer C. D., Lott B., Boisson C., Zech A., 2013, ApJ, 771, L4
Cerruti M., Zech A., Boisson C., Inoue S., 2015, MNRAS, 448, 910
Chen L., 2014, ApJ, 788, 179
Dermer C. D., Schlickeiser R., 1993, ApJ, 416, 458
Dermer C. D., Schlickeiser R., 2002, ApJ, 575, 667
Dermer C. D., Schlickeiser R., Mastichiadis A., 1992, A&A, 256, L27
Dermer C. D., Finke J. D., Krug H., Böttcher M., 2009, ApJ, 692, 32
Dermer C. D., Cerruti M., Lott B., Boisson C., Zech A., 2014, ApJ, 782, 82
Dermer C. D., Murase K., Inoue Y., 2014, J. High Energy Astrophys., 3, 29
Dermer C. D., Yan D. H., Zhang L., Finke J., Lott B., 2015, ApJ, 809, 174
Diltz C., Böttcher M., Fossati G., 2015, ApJ, 802, 133
Dimitrakoudis S., Petropoulou M., Mastichiadis A., 2014, Astropart. Phys., 54, 61
Dotson A., Georganopoulos M., Kazanas D., Perlman E. S., 2012, ApJ, 758, L15
Essey W., Kalashev O. E., Kusenko A., Beacom J. F., 2010, Phys. Rev. Lett., 104, 1102
Essey W., Ando S., Kusenko A., 2011a, Astropart. Phys., 35, 135
Essey W., Kalashev O. E., Kusenko A., Beacom J. F., 2011b, ApJ, 731, 51
Finke J. D., Dermer C. D., Böttcher M., 2008, ApJ, 686, 181
Finke J. D., Razzaque S., Dermer C. D., 2010, ApJ, 712, 238
Fossati G., Maraschi L., Celotti A., Comastri A., Ghisellini G., 1998, MNRAS, 299, 433
Franceschini A., Rodighiero G., Vaccari M., 2008, A&A, 487, 837
Gamerman D., 1997, Markov Chain Monte Carlo: Stochastic Simulation for Bayesian Inference. Chapman and Hall, London
Gelmini G. B., Kalashev O., Semikoz D. V., 2012, J. Cosmol. Astropart. Phys., 01, 044
Ghisellini G., Tavecchio F., 2009, MNRAS, 397, 958
Ghisellini G., Celotti A., Fossati G., Maraschi L., Comastri A., 1998, MNRAS, 301, 451
Ghisellini G., Tavecchio F., Maraschi L., Celotti A., Sbarrato T., 2014, Nature, 515, 376
Gu M., Cao X., Jiang D. R., 2001, MNRAS, 327, 1111
Hao L. et al., 2005, AJ, 129, 1795
Hartman R. C. et al., 1992, ApJ, 385, L1
Hayashida M. et al., 2012, ApJ, 754, 114
Hayashida M. et al., 2015, ApJ, 807, 79
Jorstad S. G., Marscher A. P., Mattox J. R., Wehrle A. E., Bloom S. D., Yurchenko A. V., 2001, ApJS, 134, 181
Jorstad S. G., Marscher A. P., Larionov V. M., 2010, ApJ, 715, 362
Kakuwa J., Toma K., Asano K., Kusunose M., Takahara F., 2015, MNRAS, 449, 551
Kalashev O. E., Kido E., 2014, preprint (arXiv:1406.0735)
Kalashev O. E., Semikoz D. V., Sigl G., 2009, Phys. Rev. D, 79, 063005
Kalashev O. E., Kusenko A., Essey W., 2013, Phys. Rev. Lett., 111, 041103
Kang S. J., Chen L., Wu Q. W., 2014, ApJS, 215, 5
Krawczynski H., 2012, ApJ, 744, 30
Liu H. T., Bai J. M., 2006, ApJ, 653, 1089
Liu H. T., Bai J. M., Wang J. M., 2011, MNRAS, 414, 155
Liu J., Yuan Q., Bi X. J., Li H., Zhang X. M., 2012, Phys. Rev. D, 85, 043507
Mackay D., 2003, Information Theory, Inference and Learning Algorithms. Cambridge Univ. Press, Cambridge
Malmrose M. P., Marscher A. P., Jorstad S. G., Nikutta R., Elitzur M., 2011, ApJ, 732, 116
Maraschi L., Ghisellini G., Celotti A., 1992, ApJ, 397, L5
Massaro E., Perri M., Giommi P., Nesci R., 2004a, A&A, 413, 489
Massaro E., Perri M., Giommi P., Nesci R., Verrecchia F., 2004b, A&A, 422, 103
Massaro F., Tramacere A., Cavaliere A., Perri M., Giommi P., 2008, A&A, 478, 395
Mastichiadis A., Petropoulou M., Dimitrakoudis S., 2013, MNRAS, 434, 2684
Mücke A., Protheroe R. J., Engel R., Rachen J. P., Stanev T., 2003, Astropart. Phys., 18, 593
Murase K., Dermer C. D., Takami H., Migliori G., 2012, ApJ, 749, 63
Murase K., Inoue Y., Dermer C. D., 2014, Phys. Rev. D, 90, 023007
Nalewajko K., Begelman M. C., Sikora M., 2014, ApJ, 789, 161
Pacciani L., Tavecchio F., Donnarumma I., Stamerra A., Carrasco L., Recillas E., Porras A., Uemura M., 2014, ApJ, 790, 45
Paliya V. S., 2015, ApJ, 808, 48
Paliya V. S., Sahayanathan S., Stalin C. S., 2015, ApJ, 803, 15
Peng Y. P., Yan D. H., Zhang L., 2014, MNRAS, 442, 2357
Pian E. et al., 1999, ApJ, 521, 112
Prosekin A., Essey W., Kusenko A., Aharonian F., 2012, ApJ, 757, 183

Downloaded from http://mnras.oxfordjournals.org/ at California Institute of Technology on January 31, 2016

Sikora M., Begelman M. C., Rees M. J., 1994, ApJ, 421, 153
Sikora M., Stawarz Ł., Moderski R., Nalewajko K., Madejski G. M., 2009, ApJ, 704, 38
Takami H., Murase K., Dermer C. D., 2013, ApJ, 771, L32
Takami H., Murase K., Dermer C. D., 2014, preprint (arXiv:1412.4716)
Tavecchio F., Ghisellini G., 2008, MNRAS, 386, 945
Tavecchio F., Maraschi L., Ghisellini G., 1998, ApJ, 509, 608
Tavecchio F., Ghisellini G., Bonnoli G., Ghirlanda G., 2010, MNRAS, 405, L94
Tramacere A., Massaro F., Cavaliere A., 2007, A&A, 466, 521
Tramacere A., Giommi P., Perri M., Verrecchia F., Tosti G., 2009, A&A, 501, 879
Tramacere A., Massaro E., Taylor A. M., 2011, ApJ, 739, 66
Weidinger M., Spanier F., 2015, A&A, 573, 7
Woo J. H., Urry C. M., 2002, ApJ, 579, 530
Yan D. H., Zhang L., 2015, MNRAS, 447, 2810
Yan D. H., Zeng H. D., Zhang L., 2012, PASJ, 64, 80
Yan D. H., Zhang L., Yuan Q., Fan Z. H., Zeng H. D., 2013, ApJ, 765, 122
Yan D. H., Zeng H. D., Zhang L., 2014, MNRAS, 439, 2933
Yan D. H., Kalashev O., Zhang L., Zhang S. N., 2015, MNRAS, 449, 1018
Yuan Q., Liu S., Fan Z., Bi X., Fryer C., 2011, ApJ, 735, 120
Zdziarski A., Böttcher M., 2015, MNRAS, 450, L21
Zhang J., Liang E. W., Zhang S. N., Bai J. M., 2012, ApJ, 752, 157
Zhang J., Zhang S. N., Liang E. W., 2013, ApJ, 767, 8
Zhou Y., Yan D. H., Dai B. Z., Zhang L., 2014, PASJ, 66, 12

APPENDIX A: FITTING RESULTS WITH LARGER SIZE OF DUST TORUS

We show the fitting results with a larger $r_{\rm dust}$, i.e. $r_{\rm dust} = 2 \times 10^{18}(L_{\rm disc}/10^{45}\ {\rm erg\ s^{-1}})^{1/2}$cm (e.g. Ghisellini et al. 2014). We then have $r_{\rm dust} \simeq 0.8$pc. Using $\tau_{\rm dust} = 0.3$, we derive $u_{\rm dust} \lesssim 2 \times 10^{-4}$ erg cm^{-3}.

Fig. A1 shows the best-fitting results with this larger $r_{\rm dust}$. One can see that the fit to the SED in period A is comparable to the fit showed in Section 3; however, the fit to lowest gamma-ray data in period C is bad in the case of the larger $r_{\rm dust}$.

In Figs A2 and A3, we show the one-dimensional probability distribution of parameter values. The mean values and the marginalized 95 per cent confidence intervals of the model parameters are reported in Table A1. In period A, a larger $\zeta_{\rm e}$ and r are required in fitting with the larger $r_{\rm dust}$. The other input parameters change little, compared with those given in Section 3. The change in $\zeta_{\rm e}$ leads to the significant changes in B' and $\delta_{\rm D}$. In period C, the input parameters are nearly identical to those reported in Section 3.

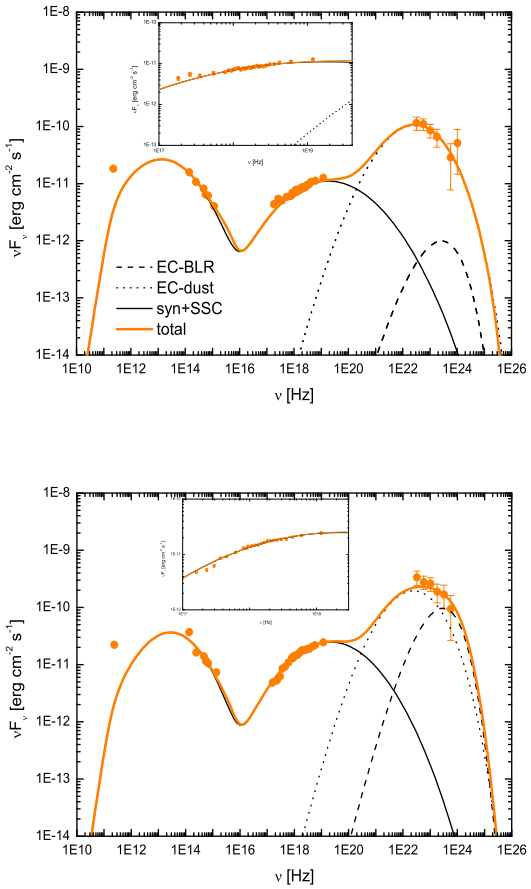

Figure A1. Best-fitting models with a larger $r_{\rm dust}$ to the SEDs of 3C 279. Upper: for period A; lower: for period C. The inset shows the details of fit at X-ray energies.

Table A1. Input and output parameters values derived in the fittings with the larger $r_{\rm dust}$. The mean values and the marginalized 95 per cent confidence intervals (CI) for interested parameters are reported.

					Input				
	$\zeta_{\rm e}$	b	L_{48}	ν_{14}	t_4	$\zeta_{\rm s}$	r (pc)	$T_{\rm dust}$ (K)	$L_{\rm disc}$ (10^{46} erg s^{-1})
Period A	3.25	1.18	0.19	0.27	5	0.48	0.7	800	0.15
(95 per cent CI)	1.52–4.91	1.11–1.26	0.17–0.20	0.23–0.31	–	0.44–0.53	0.1–1.2		–
Period C	4.58	1.50	0.24	0.52	1	0.79	0.2	800	0.15
(95 per cent CI)	3.13–4.98	1.43–1.56	0.22–0.25	0.48–0.57	–	0.71–0.87	0.1–0.3		–
					Output				
	B (G)	$\delta_{\rm D}$	$\gamma'_{\rm pk}$	$u_{\rm dust}$ (10^{-3} erg cm^{-3})	$u_{\rm BLR}$ (10^{-3} erg cm^{-3})	R' (10^{16} cm)	$P_{\rm B}$ (10^{45} erg s^{-1})	$P_{\rm r}$ (10^{46} erg s^{-1})	
Period A	0.5	23	290	0.1	0.005	3	0.9	0.6	
(95 per cent CI)	0.3–0.8	19–26	260–320	0.04–0.25	0.001–0.3	–	–	–	
Period C	1.0	29	300	0.21	0.6	0.8	0.5	1.0	
(95 per cent CI)	0.9–1.3	27–31	290–310	0.20–0.22	0.07–2	–	–	–	

Downloaded from http://mnras.oxfordjournals.org/ at California Institute of Technology on January 31, 2016

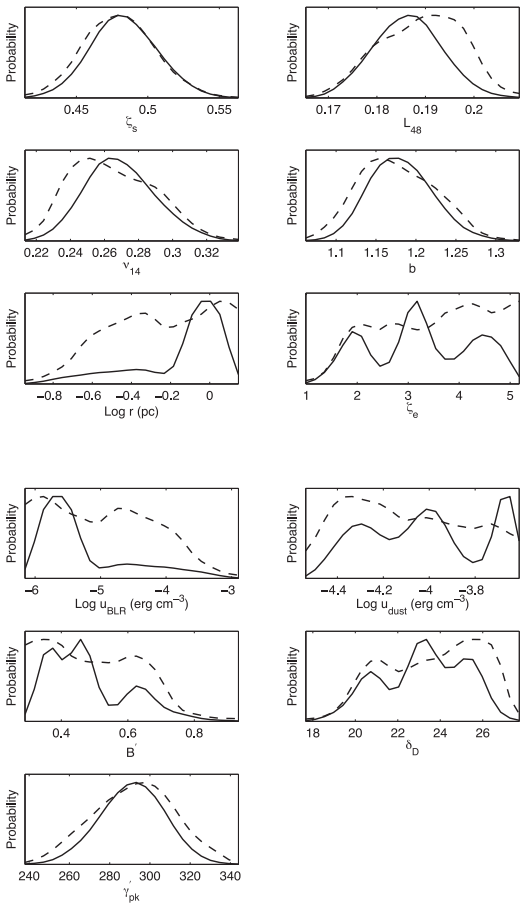

Figure A2. One-dimensional probability distribution of parameter values for period A.

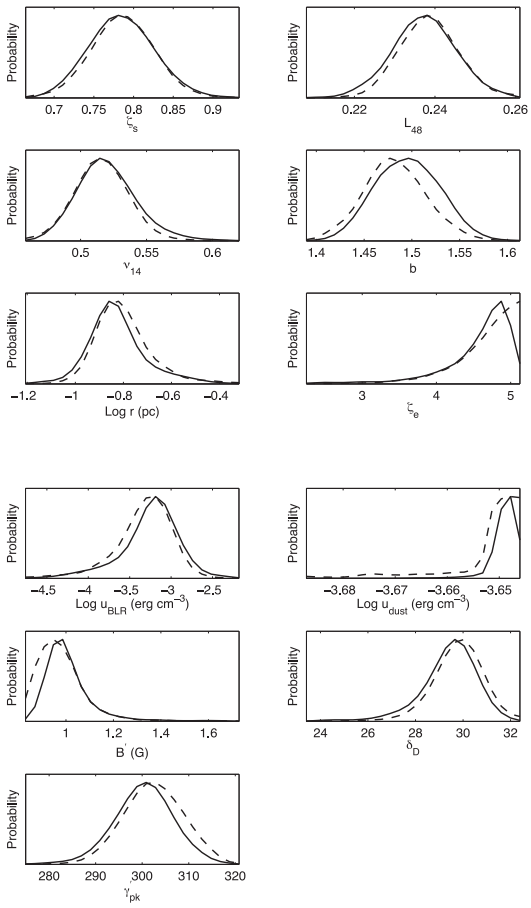

Figure A3. One-dimensional probability distribution of parameter values for period C.

This paper has been typeset from a TEX/LATEX file prepared by the author.

Downloaded from http://mnras.oxfordjournals.org/ at California Institute of Technology on January 31, 2016